

RSC Advances

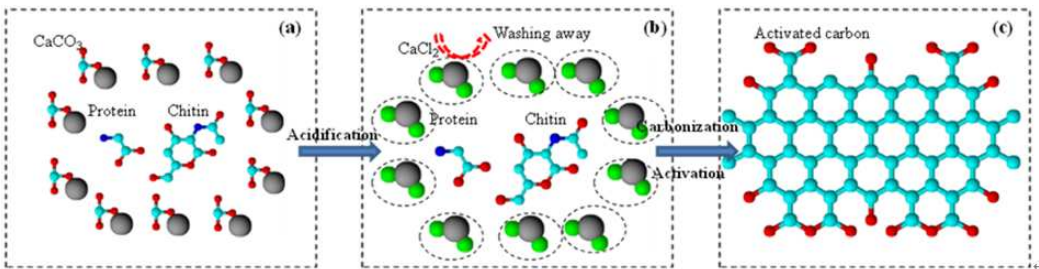


This is an *Accepted Manuscript*, which has been through the Royal Society of Chemistry peer review process and has been accepted for publication.

Accepted Manuscripts are published online shortly after acceptance, before technical editing, formatting and proof reading. Using this free service, authors can make their results available to the community, in citable form, before we publish the edited article. This *Accepted Manuscript* will be replaced by the edited, formatted and paginated article as soon as this is available.

You can find more information about *Accepted Manuscripts* in the [Information for Authors](#).

Please note that technical editing may introduce minor changes to the text and/or graphics, which may alter content. The journal's standard [Terms & Conditions](#) and the [Ethical guidelines](#) still apply. In no event shall the Royal Society of Chemistry be held responsible for any errors or omissions in this *Accepted Manuscript* or any consequences arising from the use of any information it contains.



Graphical abstract: Mechanism diagram for the synthesis of activated carbons from crab shell wastes.

High surface area and oxygen-enriched activated carbon synthesized from animal cellulose and evaluated in electric double-layer capacitors

Yuan Gao, Qinyan Yue^{*}, Baoyu Gao

Shandong Provincial Key Laboratory of Water Pollution Control and Resource Reuse,
School of Environmental Science and Engineering, Shandong University, Jinan
250100, China

^{*} Corresponding author. Tel.: +86 531 88365258; fax: +86 531 88364513

E-mail address: qyyue58@aliyun.com.

Abstract

Crab shell, an abundant food waste and high volume organic resource, has been used to synthesize oxygen-enriched activated carbon. The thermal stability, surface area, morphology and surface chemical composition were characterized by thermogravimetric analysis, nitrogen adsorption, scanning electron microscope, energy dispersive X-ray spectroscopy, Fourier transform infrared spectroscopy and X-ray photoelectron spectroscopy. The obtained activated carbon had a high surface area of 3442 m² g⁻¹, large pore volume of 2.327 cm³ g⁻¹ and rich surface oxygen species of 18.50 at.%. The cyclic voltammogram, galvanostatic charge/discharge and electrochemical impedance spectroscopy tests were performed to investigate the electrochemical properties of resultant carbon electrodes. The specific capacitance was 280.6 F g⁻¹ at a current density of 0.2 A g⁻¹ and still maintained as high as 233.4 F g⁻¹ even at a high current density of 10 A g⁻¹, indicating the great potential of crab

1 shell-activated carbons in the development as electrode materials for
2 high-performance supercapacitors.

3 **Keywords:** Activated carbon; Animal cellulose; High surface area; Oxygen-enriched;
4 Electrochemical properties

5 **1. Introduction**

6 There are huge amount of lakes and oceans all over the world, therefore the
7 production of crabs is enormous per year ¹. Crab shells (CS) are one of the most
8 common solid wastes in seafood industries. Based on up-to-date data, it is estimated
9 that the production of crab shell is over millions of tons annually and approximately
10 85% of crab shells are ultimately disposed in landfill, resulting in a serious
11 environmental problem. Owing to the strict environmental regulations, how to reuse
12 this solid waste in a proper manner and also create possible economic value to the
13 industries is significant. The raw crab shells are mainly composed of 40-60% calcium
14 carbonate, 20-27% chitin, 11-29% protein, 3-5% magnesium carbonate and some
15 lipids as dry weight basis ²⁻⁴. Chitin, the second most abundant polymer in nature, can
16 be extracted from the shells by using very simple chemical treatments. Chitin is a
17 modified polysaccharide with a strictly hierarchical structure, which is consisted of
18 the units of N-acetylglucosamine ⁵. Or rather, chitin could be regarded as one
19 hydroxyl group on per monomer of cellulose replaced by an acetyl amine group.
20 Chitin, also called animal cellulose, possess abundantly available carbon content and
21 various surface chemical groups. In addition, chitin in crab shell is often associated
22 with various types of proteins or lipids, which could also be employed as carbon

1 precursor.

2 Up to now, most researches have been only focused on the reutilization of crab
3 shells or chitin from crab shells as bioadsorbents to remove heavy metals ⁶⁻⁹.
4 Activated carbons (ACs) with high surface area, large pore volume and hierarchical
5 microporous/mesoporous structure are widely used in various fields, including
6 adsorption ¹⁰, gas separation/ storage ^{11, 12}, catalysis supporter ¹³ and electric
7 double-layer capacitors (EDLCs) ¹⁴. However, the commercial ACs derived from
8 relatively expensive and non-renewable starting materials such as coals, are high cost
9 and unjustified to the pollution control applications. Recently, various types of wastes
10 have proven to be good candidates for the synthesis of ACs, such as nut shell ¹⁵,
11 sludge ¹⁶, alkali lignin ¹⁷, lotus stalk ¹⁸, coal tar pitch ¹⁹, rice husk ²⁰ and
12 *Enteromorpha prolifera* ²¹. Animal cellulose from crab shell wastes could also be an
13 available raw material for the synthesis of ACs.

14 According to literature reviews, no research has been reported on the preparation
15 of low-cost activated carbon from animal cellulose of crab shells. Therefore, the main
16 objective of this study was to explore the potential of crab shell wastes in the
17 synthesis of activated carbon with high surface area using potassium hydroxide as
18 activating agent. The physical/ chemical properties and electrochemical performances
19 of the obtained ACs were also investigated.

20 **2. Experimental**

21 **2.1. Preparation of activated carbon**

22 Raw crab shell wastes were collected from a crabmeat processing factory in Hebei,

1 China. The shells were sun-dried for several days and mechanically ground to
2 particles in size range of 0.074-0.15 mm. As shown in Fig. 1 and Fig. 2, the formation
3 process of the ACs from crab shells was carried out on a simple and reproducible
4 route. Firstly, the raw shell was treated with 1 N HCl at a solid-liquid ratio of 100 g
5 L⁻¹ for 6 h followed by rinsing with distilled water several times. This pre-treatment
6 procedure was performed to guarantee the removal of excess minerals, like calcium
7 carbonate or calcium phosphate, on the shell surface^{22,23}. The obtained acidified crab
8 shell (ACS) was mainly composed of chitin and protein. Then, the ACS was dried in
9 an oven at 60 °C for 24 h and the weight loss in this process was found to be
10 approximately 55 ± 1%. Secondly, the ACS was carbonized at 500 °C for 90 min. The
11 obtained char was denoted as CCS. The char yield in the carbonation process was 28
12 ± 0.5%. Then the CCS was mixed with potassium hydroxide powder. The mixture
13 was transferred to a tube furnace and pyrolyzed under nitrogen flow at 800 °C for 60
14 min. After cooling under nitrogen protection, the sample was washed repeatedly with
15 HCl solution and distilled water to remove residual alkali and inorganic impurities.
16 Finally, the product was dried at 105 °C overnight and ground into powders. The
17 obtained product was designated as CSAC-x (x=1, 2, 3, 4 and 5), where x represented
18 the weight ratio between potassium hydroxide and char. The carbon yield in the
19 activation process was 24.5 ± 1%. This preparation process was referred from our
20 previous work²¹. The synthesis process was carried out in triplicate and the average
21 result was obtained.

22 2.2. Characterization

1 Thermal gravimetric analysis (TGA) was performed using a thermogravimetric
2 analyzer (SHI-MADZU, TGA-50). Each analysis was carried out at a 100 mL min⁻¹
3 N₂ rate with a heat rate of 10 °C min⁻¹ from room temperature to 900 °C. The pore
4 size distribution and surface area of the ACs were determined at 77 K using a surface
5 area analyzer (JW-BK122W). The surface physical morphology and mineral
6 components of the ACs were examined by using a scanning electron microscopy
7 (JEOL, JSM 7600F) and an energy dispersive X-ray spectroscopy (Oxford INCA
8 sightX). Fourier transform infrared spectroscopy (NICOLET 6700) and X-ray
9 photoelectron spectroscopy (ESCALAB 250) tests were carried out to investigate the
10 chemical properties of the samples.

11 **2.3. Electrochemical measurements**

12 All electrochemical characterizations of the CSAC-3 based electrodes were tested
13 in a symmetrical two-electrode configuration with 6 M KOH as electrolyte using an
14 electrochemical workstation (PARSTAT2273). To make a work electrode, the active
15 CSAC-3 powder, acetylene black and polytetrafluoroethylene (PTFE) were mixed in
16 ethanol with a weight ratio of 85: 15: 5. The mixture was coated onto nickel foam like
17 a sandwich with an area of 1 cm² and pressed under a pressure of 10 MPa. The
18 electrodes were dried in a vacuum oven at 100 °C overnight. Approximately 2 mg of
19 active material was loaded in each electrode, and each electrode layer thickness was
20 50 μm. Electrochemical performances of the prepared carbon electrodes were
21 evaluated by cyclic voltammetry (CV), galvanostatic charge-discharge (GCD) and
22 electrochemical impedance spectroscopy (EIS). The potential window of CV curve

was set to be 0-1.0 V. In GCD test, different current densities from 0.2 to 10 A g⁻¹ were employed to evaluate the charge-discharge performance of the samples. The EIS test was performed in the frequency ranges of 100 kHz to 100 mHz at an open circuit potential of 10 mV. The specific capacitance based on CV and GCD measured was calculated using the following equations:

$$C_{cv} = \frac{\int I du}{vm\Delta V} \quad (1)$$

$$C_{gcd} = \frac{I\Delta t}{m\Delta V} \times 2 \quad (2)$$

where I is the current (A), u is the potential (V), v is the voltage scan rate (mV s⁻¹), m is the weight of the active material in each electrode, ΔV is the total potential difference (V) and Δt is the discharge time (s).

3. Results and discussion

3.1. Thermal analysis

TGA analysis can provide useful information on thermal behavior of materials through the study of characteristic decomposition patterns or degradation mechanisms. Hence, TGA coupled with DTG analysis were employed in this study to gain suitable temperature range for the carbonization and activation process. Fig. 3 exhibits the TGA-DTG curves for both acidified crab shell and carbonized crab shell impregnated with KOH. Both samples display three steps for weight loss, yet remarkable variations could be discovered in the band locations and intensities. Fig. 3a shows that the decomposition of the acidified crab shell was consisted of three stages, namely dehydration, devolatilization and decomposition of carbonaceous substance, which

1 was different from pure chitin or protein^{24, 25}. This result demonstrated that the
2 acidified crab shell was a combination of chitin, protein, lipid, ash and moisture,
3 which was in agreement with the previous study²³. Furthermore, the shape of TGA
4 curve of acidified crab shell resembled like that of cellulose, implying that the
5 obtained acidified material could be used as a promising carbon precursor^{26, 27}. The
6 first mass loss of 11.44% at 30-200 °C was caused by the evaporation of water
7 molecules, while the second mass loss observed in the temperature range of 200-408
8 °C was a result of the decomposition of chitin, protein or lipid molecules.
9 Approximately 53.03% weight of the sample was lost during this stage with two
10 significant DTG peaks at about 317.5 and 384.6 °C, which were similar to previous
11 studies^{24, 25, 28}. In the third stage, from 408 to 800 °C, the sample release 15.77%
12 volatile substances and a char residue of 19.76% was gained. According to the above
13 analysis, the carbonization temperature was selected at 500 °C, because large
14 proportion of dehydration and devolatilization of raw materials occurred in this stage.

15 On the other hand, the raw precursor could be eroded by potassium hydroxide and
16 produced pores in the following aspects. (a) The primary surface dehydration
17 occurred, which could be deduced from the DTG peak at 77.2 °C (Fig. 3b). (b) The
18 secondary evaporation of internal water and partial polymerization of the raw
19 precursor were deduced from the DTG peak at 209.8 °C. (c) The raw precursor
20 transformed to char through aromatization reaction, which presented a high weight
21 loss between the temperature 100 and 750 °C. During this stage, the metallic
22 potassium coupled with some carbonates were produced to yield abundant fine pores

1 through intercalating to the carbon matrix ²⁹. (d) The progressive weight loss above
2 750 °C was attributed to the decomposition of potassium carbonate into CO₂.
3 Therefore, the activation temperature was set at 800 °C to ensure good development
4 of pores.

5 **3.2. Pore and microstructure characterization**

6 It can be seen from Table S1 that raising the impregnation ratio from 1 to 3 lead to
7 an increase in BET surface area from 1782 to 3442 m² g⁻¹, while further raising the
8 impregnation ratio from 3 to 5 resulted in a decrease in BET surface area from 3442
9 to 2188 m² g⁻¹. CSAC with the highest surface area was obtained at the impregnation
10 ratio of 3. Therefore, CSAC-3 was regarded as a typical sample for the following
11 investigation. As shown in Fig. 4a, the N₂ adsorption-desorption isotherms of
12 CSAC-3 presented a type I shape with somewhat type IV character. The isotherms
13 showed a significant adsorption of nitrogen at the relative pressure below 0.1,
14 indicating the presence of micropores. A slight hysteresis loop (or capillary
15 condensation) occurred at the medium relative pressure of 0.4-0.7, implying that
16 CSAC-3 possessed some mesopores. And the hysteresis loop belonged to H3/H4,
17 which was associated to the existence of slit-like pores ^{30,31}. The size of micropores
18 for CSAC-3 displayed a multimodal distribution nature with four different maxima at
19 0.55, 0.62, 0.74 and 0.83 nm (Fig. 4b). All textural parameters of CS, ACS, CCS and
20 CSAC-3 are presented in Table 1. The acidification and carbonization processes led to
21 slight change to the surface area and pore volume for raw precursor. However, the
22 surface area and pore volume increased to 3442 m² g⁻¹ and 2.327 cm³ g⁻¹ after

1 activation. Compared with some previous studies³²⁻³⁵, ACs prepared from crab shell
2 exhibited higher surface area than that of other raw precursors, such as sugarcane
3 molasses, sunflower seed shell, rice straw and *Argania spinosa* seed shells. The
4 average pore diameter for CSAC-3 was 2.704 nm and the ratio of mesopores/ total
5 pores reached 90.46%. As displayed in Fig. 4b, most pores were intensively
6 distributed in the pore range of 2-4 nm. According to the previous study, large surface
7 area and high proportion of mesopores for ACs facilitated the access of electrolyte
8 ions into the pores, contributing to good electrochemical performances in EDLCs³⁶,
9³⁷.

10 Scanning electron microscopy equipped with EDX was carried out to analyze the
11 morphologies and components on the surface of CS, ACS, CCS and CSAC-3. In EDX
12 analysis (Fig. 5), strong Ca peaks could be observed on virgin crab shell surface,
13 which confirmed that the shells contained calcium carbonate. Other peaks
14 corresponding to Na, Mg, P, Cl, K, Cu, Mn and Pb were also recorded in the EDX
15 spectrum (Table S2). It is interesting to find that the calcium peaks decreased
16 remarkably after acidification, implying that the calcium leached out from the shells
17 successfully through demineralization. SEM images showed that the surface of virgin
18 crab shell display lamellar-like structure with many straightly tunnel-like and striped
19 trench (Fig. 6a and Fig. S1a). After acidification treatment, the ACS surface exhibited
20 apparent microfibrillar crystalline structure in a sequence of hierarchical layer patterns,
21 indicating that the reserved main constituents contained chitin (Fig. 6b and Fig. S1b).
22 Other previous researchers also found that the purified crab shell displayed similar

microfibrillar structure^{5, 38}. After carbonization, the surface became smooth with plate-like stripes (Fig. 6c and Fig. S1c). After activation, the surface of the resultant sample presented abundantly flower-like or honeycomb-like 3-D pore network skeleton (Fig. 6d and Fig. S1d).

3.3. Chemical characterization

The electrochemical behaviors of EDLCs not only rely on the physical properties but also on surface chemical characteristics, hence FTIR and XPS were used in this study. Fig. 7 revealed five different characteristic bands for CS, ACS, CCS and CSAC-3. These bands were: 3425 cm⁻¹ (O-H stretching vibration), 2910 cm⁻¹ (C-H stretching), 1648 cm⁻¹ (C=O secondary amide stretching), 1425 cm⁻¹ (C-H deformation) and 1060 cm⁻¹ (O-C-O asymmetric stretching in phase ring)^{24, 39}, which became weaken, shifted or disappeared for CSAC-3, indicating that the hydrogen element was removed to a large extent due to the dehydration or pyrolyzation reaction during activation process. The surface elemental compositions of the prepared carbon were further evaluated by XPS, listed in Fig. S2. It can be seen that the C1s spectrum could be deconvoluted into three components, corresponding to: graphite type (284.6 eV), carbon in phenolic, alcoholic, etheric groups (285.6 eV) and carbon in carboxyl or ester groups (288.7 eV)^{39, 40}. The O1s spectra could be resolved into three individual component peaks: oxygen in hydroxyl or metal oxides (530.6 eV), oxygen doubly bonded to carbon (532.4 eV) and oxygen singly bonded to carbon in aromatic rings, phenols and ethers (533.1 eV)^{40, 41}. According to the area-simulating curve, the relative percentage of each component was calculated and summarized in Table 2.

The relative content of oxygen in aromatic rings, phenols and ethers was 7.60%, which was very high. According to the previous studies, CO-type functional groups on the surface of ACs, including hydroxyl, quinone, phenols, ethers and carbonyl groups, had a positive contribution to the specific capacity of carbon electrodes⁴²⁻⁴⁴. Since large numbers of O-enriched functional groups could not only promote the wettability of carbon material, thus favouring the electrolyte ions to contact with the pores, but also provide an additional pseudocapacitance due to a faradic process involving the oxygen groups^{42, 43}.

3.4. Electrochemical behavior

Fig. 8a presents the CV curves of CSAC-3 electrodes at various scan rates of 10-100 mV s⁻¹ in 6 M KOH aqueous electrolyte. The CSAC-3 electrodes displayed good rectangular shapes, exhibiting almost mirror images with reference to the zero-current line, which was a typical characteristic of the EDLCs. Furthermore, the rectangular degree of the curves presented the ion diffusion rate into the pores of the electrodes, and the higher rectangular degree reflects bigger ion diffusion rate³⁶. Hence, the high rectangular degree of CV curves at high scan rates in this study corresponded to the good ion transfer properties of the CSAC-3 electrode materials. It is well-known that the RC time constant (τ) of the electrode is an important influence factor on the voltammogram shape. The larger the constant time is, the longer the transient part (less steepness of the CV curves at the switching potential) will be, which signifies worse collapse of the rectangular profiles^{37, 45, 46}. In addition, this phenomenon usually becomes more prominent at higher scan rates. In this study, the

CV curves still maintained a good box-like shape at high scan rates, which implied that the carbon electrode had small constant time as a desired capacitor with an excellent capacitive ability. The RC time constant is only 5.01 s, which indicated that the CSAC-3 electrode was suitable for higher power delivery.

The galvanostatic charge/discharge measurement at different current densities was further employed to explore the electrochemical behaviors of the electrode materials. All galvanostatic charge/discharge curves show almost isosceles triangular in shape even at high current density of 2.5 A g^{-1} (Fig. 8b), suggesting an ideal electrochemical reversibility of the electrodes. Additionally, the specific capacitance of CSAC-3 electrodes was 280.6 F g^{-1} at a current density of 0.2 A g^{-1} and still remained as high as 233.4 F g^{-1} when the current density increased up to 10 A g^{-1} (Fig. 8c), which is comparable to those reported elsewhere^{19, 20, 37, 45}. The decrease of the capacitance mainly derived from ohmic drop or high polarization of electrode at high current density, which could result from the weakening accessibility of ions into the pores of electrode matrices with the increasing current density³⁶. The high capacitance retention of 83% reflected an excellent rate capability of the electrodes.

To evaluate the effects of frequency on the power performance of CSAC-3 electrodes, the prepared carbon electrodes were investigated by electrochemical impedance spectroscopy. As shown in Fig. 9 a, the Nyquist plot consist of three parts: (a) a semicircle at high frequency region, which was correlated to the resistance of the CSAC-3 electrode itself as well as the contact resistance between CSAC-3 electrode and current collector. During this stage, the value of capacitance was almost zero and

1 the system behaved like a pure resistor (Fig. 9b). Because scarcely any charge transfer
2 complexes could overcome the activation energy to move with the quick changes of
3 the potential; (b) a 45° Warburg line at middle frequency region served as a knee or
4 transition between the semicircle and vertical line; (c) a vertical line at low frequency
5 region implied a pure capacitive electric double layer capacitor behavior^{31, 36}. The
6 data of Nyquist curve was fitted by using the ZSimpWin software based on the
7 equivalent circuit (Fig. 9a inset). The equivalent series resistance of the electrode was
8 0.194 Ω , which made it possible for high power performance. The excellent
9 electrochemical performance of CSAC-3 electrode may attribute to the characteristics
10 of the crab shell carbon materials. Firstly, large specific surface area provided
11 sufficient electrode/electrolyte interface sites for charge storage. Secondly, dominant
12 mesopores in the porous carbon material resulted in low inner-pore ion-transport
13 resistance and diffusion distance, which facilitated the electrolyte ion to transfer and
14 access into the internal pores quickly^{37, 47}. Thirdly, the presence of abundant
15 oxygen-contained groups enhanced the surface wettability of the electrode surface,
16 affording more exposed surface for charge accommodation.

17 **4. Conclusions**

18 Novel oxygen-rich activated carbons were fabricated by KOH activation using
19 animal cellulose withdrawn from crab shell wastes as precursor and applied as
20 electrode materials. The obtained carbon materials presented outstanding performance
21 as an EDLC electrode owing to large specific surface area of 3442 $\text{m}^2 \text{g}^{-1}$, high
22 mesopores ratio of 90.46% and high oxygen content of 18.50%. The advantages of the

1 raw material were: (1) abundantly available and cheap; (b) instinctively high oxygen
2 content; (c) simple and cost-effective synthesis; (d) good electrochemical performance.
3 This investigation provides an interesting and promising candidate for supercapacitor
4 industry.

5 **Appendix A. Supplementary data**

6 Supplementary data related to this article can be found, in the online version, at

7 **References**

- 8 1. D. S. Kim, *Bioresour. Technol.*, 2004, 94, 345-348.
- 9 2. K. Vijayaraghavan, H. Y. N. Winnie and R. Balasubramanian, *Desalination*, 2011,
10 266, 195-200.
- 11 3. S. Lu, S. W. Gibb and E. Cochrane, *J. Hazard. Mater.*, 2007, 149, 208-217.
- 12 4. K. Vijayaraghavan, K. Palanivelu and M. Velan, *Bioresour. Technol.*, 2006, 97,
13 1411-1419.
- 14 5. M.-T. Yen, J.-H. Yang and J.-L. Mau, *Carbohydrate Polym.*, 2009, 75, 15-21.
- 15 6. E. I. Cadogan, C.-H. Lee, S. R. Popuri and H.-Y. Lin, *In. Biodeter. Biodegr.*, 2014,
16 95, 232-240.
- 17 7. K. Vijayaraghavan and R. Balasubramanian, *Chem. Eng. J.*, 2010, 163, 337-343.
- 18 8. I. B. Rae, S. W. Gibb and S. Lu, *J. Hazard. Mater.*, 2009, 164, 1601-1604.
- 19 9. P. X. Pinto, S. R. Al-Abed and D. J. Reisman, *Chem. Eng. J.*, 2011, 166,
20 1002-1009.
- 21 10. M. Houari, B. Hamdi, O. Bouras, J.-C. Bollinger and M. Baudu, *Chem. Eng. J.*,
22 2014, 255, 506-512.

- 1 11. K. Kante, C. Nieto-Delgado, J. R. Rangel-Mendez and T. J. Bandosz, *J. Hazard.*
2 *Mater.*, 2012, 201-202, 141-147.
- 3 12. N. Ferrera-Lorenzo, E. Fuente, I. Suárez-Ruiz and B. Ruiz, *Chem. Eng. J.*, 2014,
4 250, 128-136.
- 5 13. L. L. Bo, Y. B. Zhang, X. Quan and B. Zhao, *J. Hazard. Mater.*, 2008, 153,
6 1201-1206.
- 7 14. S. Kumagai, M. Sato and D. Tashima, *Electrochim. Acta*, 2013, 114, 617-626.
- 8 15. A. C. Martins, O. Pezoti, A. L. Cazetta, K. C. Bedin, D. A. S. Yamazaki, G. F. G.
9 Bandoch, T. Asefa, J. V. Visentainer and V. C. Almeida, *Chem. Eng. J.*, 2015,
10 260, 291-299.
- 11 16. P. Hadi, M. Xu, C. Ning, C. Sze Ki Lin and G. McKay, *Chem. Eng. J.*, 2015, 260,
12 895-906.
- 13 17. S. Hu, S. Zhang, N. Pan and Y.-L. Hsieh, *J. Power Sources*, 2014, 270, 106-112.
- 14 18. H. Liu, W. Liu, J. Zhang, C. Zhang, L. Ren and Y. Li, *J. Hazard. Mater.*, 2011, 185,
15 1528-1535.
- 16 19. X. He, H. Zhang, H. Zhang, X. Li, N. Xiao and J. Qiu, *J. Mater. Chem. A*, 2014, 2,
17 19633.
- 18 20. X. He, P. Ling, J. Qiu, M. Yu, X. Zhang, C. Yu and M. Zheng, *J. Power Sources*,
19 2013, 240, 109-113.
- 20 21. Y. Gao, W. Zhang, Q. Yue, B. Gao, Y. Sun, J. Kong and P. Zhao, *J. Power Sources*,
21 2014, 270, 403-410.
- 22 22. C. H. Niu, B. Volesky and D. Cleiman, *Water Res.*, 2007, 41, 2473-2478.

- 1 23. H. Niu and B. Volesky, *Hydrometallurgy*, 2006, 84, 28-36.
- 2 24. M. Kaya, O. Seyyar, T. Baran, S. Erdogan and M. Kar, *Int. J Biol. Macromol.*,
3 2014, 65, 553-558.
- 4 25. K. Kebelmann, A. Hornung, U. Karsten and G. Griffiths, *Biomass Bioenergy*, 2013,
5 49, 38-48.
- 6 26. P. R. Sharma and A. J. Varma, *Carbohydr Polym*, 2014, 114, 339-343.
- 7 27. Q. Liu, Z. Zhong, S. Wang and Z. Luo, *J. Anal. Appl. Pyrolysis*, 2011, 90,
8 213-218.
- 9 28. M. Kaya, S. Erdogan, A. Mol and T. Baran, *Int. J Biol. Macromol.*, 2015, 72,
10 797-805.
- 11 29. A.-N. A. El-Hendawy, *Appl. Surf. Sci.*, 2009, 255, 3723-3730.
- 12 30. M. E. Fernandez, G. V. Nunell, P. R. Bonelli and A. L. Cukierman, *Ind.Crop. Prod.*,
13 2014, 62, 437-445.
- 14 31. Q. Wang, J. Yan, Y. Wang, T. Wei, M. Zhang, X. Jing and Z. Fan, *Carbon*, 2014,
15 67, 119-127.
- 16 32. A. H. Basta, V. Fierro, H. El-Saied and A. Celzard, *Bioresour. Technol.*, 2009, 100,
17 3941-3947.
- 18 33. A. Elmouwahidi, Z. Zapata-Benabithé, F. Carrasco-Marin and C. Moreno-Castilla,
19 *Bioresour. Technol.*, 2012, 111, 185-190.
- 20 34. X. Li, W. Xing, S. Zhuo, J. Zhou, F. Li, S. Z. Qiao and G. Q. Lu, *Bioresour.*
21 *Technol.*, 2011, 102, 1118-1123.
- 22 35. J. Sreńscek-Nazzal, W. Kamińska, B. Michalkiewicz and Z. C. Koren, *Ind.Crop.*

- 1 *Prod.*, 2013, 47, 153-159.
- 2 36. M. Wu, P. Ai, M. Tan, B. Jiang, Y. Li, J. Zheng, W. Wu, Z. Li, Q. Zhang and X. He,
3 *Chem. Eng. J.*, 2014, 245, 166-172.
- 4 37. W. Zhang, Z.-H. Huang, G. Cao, F. Kang and Y. Yang, *J. Power Sources*, 2012,
5 204, 230-235.
- 6 38. O. C. Wilson, A. Gugssa, P. Mehl and W. Anderson, *Mater. Sci. Eng., C*, 2012, 32,
7 78-82.
- 8 39. H. Liu, X. Wang, G. Zhai, J. Zhang, C. Zhang, N. Bao and C. Cheng, *Chem. Eng.*
9 *J.*, 2012, 209, 155-162.
- 10 40. Artur P. Terzyk, *Colloids Surface A.*, 20011, 77, 23-45.
- 11 41. S. Altenor, B. Carene, E. Emmanuel, J. Lambert, J.-J. Ehrhardt and S. Gaspard, *J.*
12 *Hazard. Mater.*, 2009, 165, 1029-1039.
- 13 42. V. Ruiz, C. Blanco, E. Raymundo-Piñero, V. Khomenko, F. Béguin and R.
14 Santamaría, *Electrochim. Acta*, 2007, 52, 4969-4973.
- 15 43. M. J. Bleda-Martínez, J. A. Maciá-Agulló, D. Lozano-Castelló, E. Morallón, D.
16 Cazorla-Amorós and A. Linares-Solano, *Carbon*, 2005, 43, 2677-2684.
- 17 44. H. Oda, A. Yamashita, S. Minoura, M. Okamoto and T. Morimoto, *J. Power*
18 *Sources*, 2006, 158, 1510-1516.
- 19 45. H.-Q. Li, Y.-G. Wang, C.-X. Wang and Y.-Y. Xia, *J. Power Sources*, 2008, 185,
20 1557-1562.
- 21 46. S. Yoon, J. Lee, T. Hyeon, S.-M. Oh, *J. Electrochem. Soc.*, 2000, 147 (7),
22 2507-2512.

1 47. J. Wang, M.-M. Chen, C.-Y. Wang, J.-Z. Wang, J.-M. Zheng, *J. Power Sources*,
2 2011, 196, 550-558.

3
4
5
6
7
8
9
10
11
12
13
14
15
16
17
18
19
20
21
22

RSC Advances Accepted Manuscript

Figure captions

- Fig. 1. Flow diagram for the synthesis of activated carbons from crab shell wastes.
- Fig. 2. Mechanism diagram of for the synthesis of activated carbons from crab shell wastes.
- Fig. 3. TGA and DTG curves for the pyrolysis of (a) acidized crab shell and (b) carbonized char impregnated with potassium hydroxide.
- Fig. 4. (a) N₂ sorption/desorption isothermals and (b) pore size distribution curves (inset: micropore size distribution) of the prepared carbons.
- Fig. 5. EDX spectrum (a) raw crab shell and (b) acidized crab shell.
- Fig. 6. Scanning electron microscopy image of (a) raw crab shell, (b) acidized crab shell, (c) carbonized crab shell and (d) crab shell activated carbon ($\times 20000$).
- Fig. 7. FTIR spectra of (a) raw crab shell, (b) acidized crab shell, (c) carbonized crab shell and (d) crab shell activated carbon.
- Fig. 8. (a) Cyclic voltammograms at different scan rates, (b) charge/discharge curves and (c) the specific capacitance at various current densities of CSAC-3 electrodes.
- Fig. 9. (a) Nyquist impedance plots and normalized real and imaginary part capacitance of the CSAC-3 electrodes.
- Fig. S1. Scanning electron microscopy image of (a) raw crab shell, (b) acidized crab shell, (c) carbonized crab shell and (d) crab shell activated carbon ($\times 5000$).
- Fig. S2. C 1s and O 1s XPS spectra of CSAC-3.

Table 1
Porous structure parameters of crab shell, acidized crab shell, carbonized crab shell and crab shell
resulting activated carbon.

Parameters	CS	ACS	CCS	CSAC-3
BET surface area ($\text{m}^2 \text{g}^{-1}$)	1.817	5.061	10.45	3442
Total pore volume ($\text{cm}^3 \text{g}^{-1}$)	0.030	0.017	0.033	2.327
<i>t</i> -method micropore volume ($\text{cm}^3 \text{g}^{-1}$)	0.000	0.000	0.000	0.642
BJH method mesopore volume ($\text{cm}^3 \text{g}^{-1}$)	0.033	0.019	0.036	2.105
Average pore diameter (nm)	65.479	13.753	12.744	2.704

1 Table 2

2 Relative content of the surface functional groups determined from the XPS analysis.

	Peaks no.	Binding energy (eV)	Surface group	Assignment	Relative content (%)
C1s	Peak 1	284.6	C	Graphitic carbon	35.92
	Peak 2	285.6	C-O-	Phenolic, alcoholic, etheric	20.10
	Peak 3	288.7	COO	Carboxyl or ester	24.21
O1s	Peak 1	530.6	O/OH-	Hydroxyl or metal oxides	0.63
	Peak 2	532.4	C=O	Oxygen doubly bonded to carbon	10.27
	Peak 3	533.1	C-O-	Aromatic rings, in phenols and ethers	7.60
N1s	Peak 1	400.2	C-N-C	Pyrrolic nitrogen, pyridones or a mixture of both	1.27

3

4

5

6

7

8

9

10

11

12

13

14

15

16

17

18

19

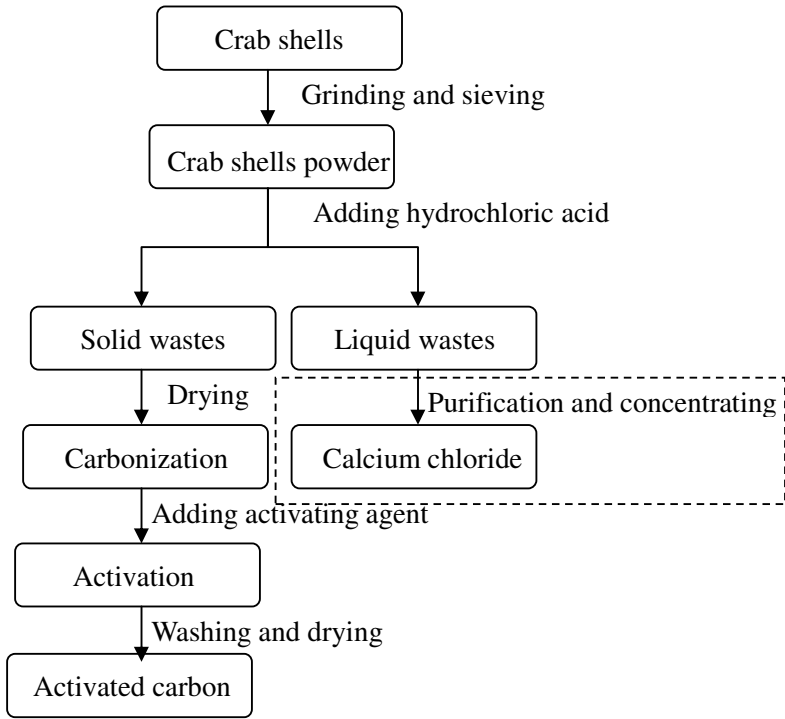


Fig. 1. Flow diagram for the synthesis of activated carbons from crab shell wastes.

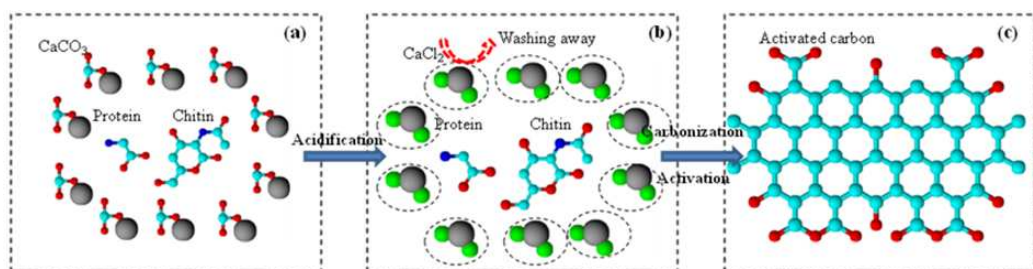


Fig. 2. Mechanism diagram for the synthesis of activated carbons from crab shell wastes.

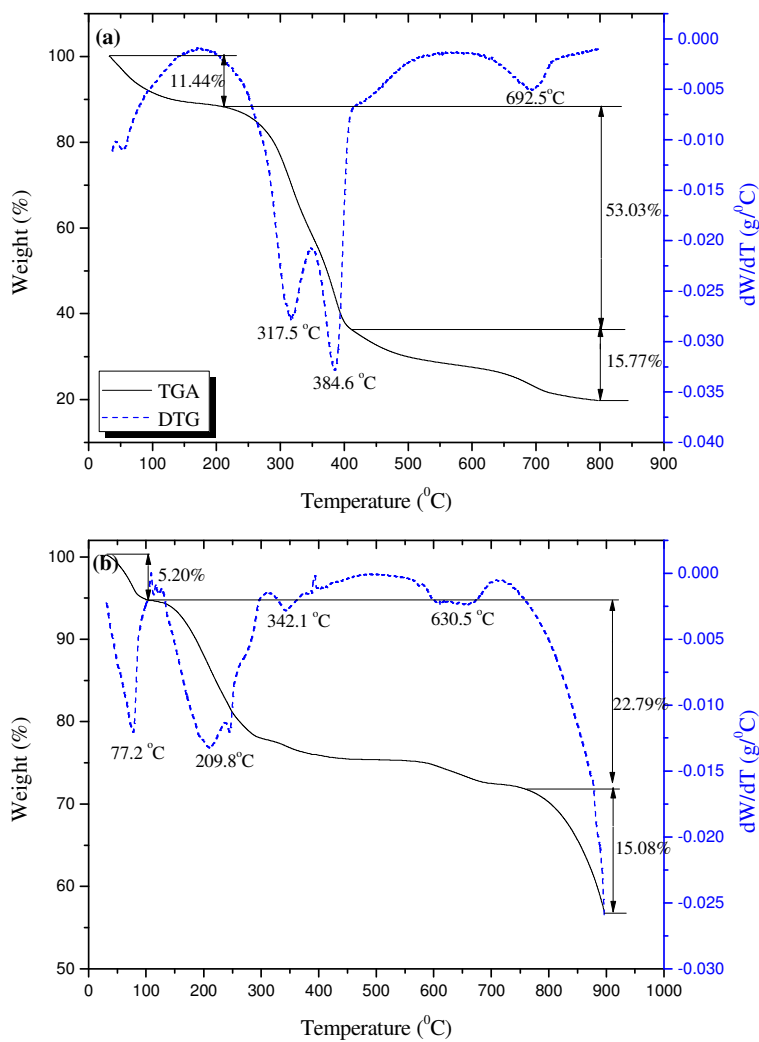


Fig. 3. TGA and DTG curves for the pyrolysis of (a) acidized crab shell and (b) carbonized char impregnated with potassium hydroxide.

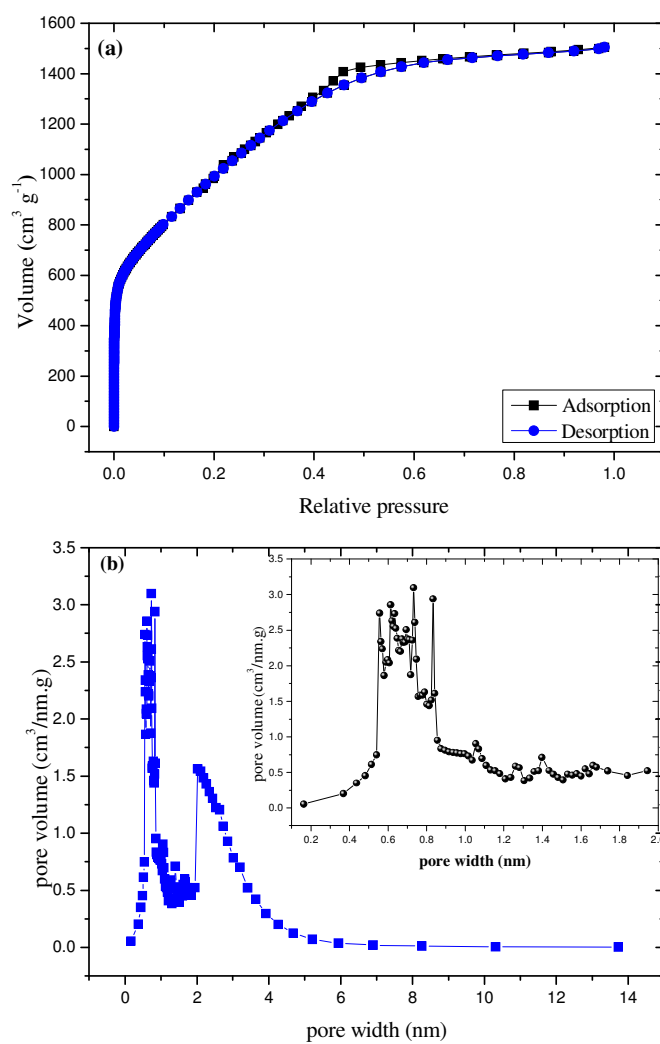


Fig. 4. (a) N_2 sorption/desorption isotherms and (b) pore size distribution curves (inset: micropore size distribution) of crab shell activated carbon.

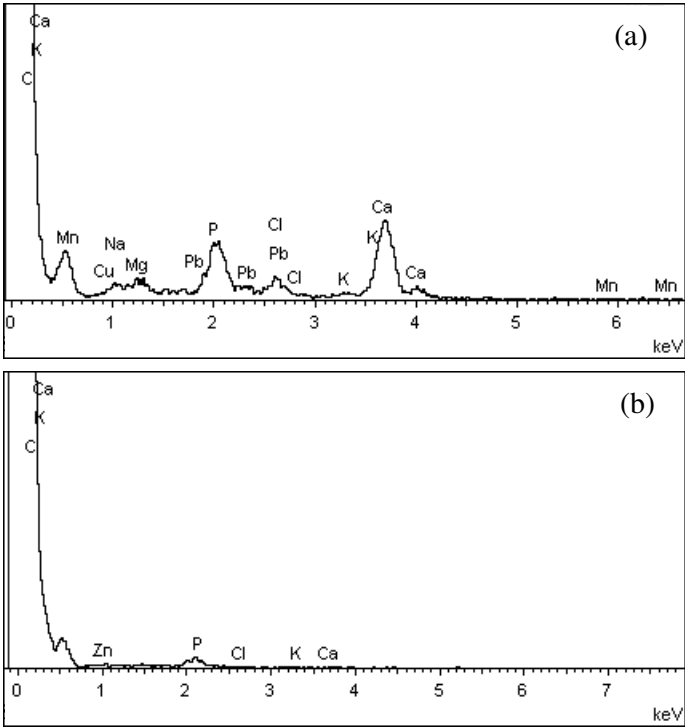


Fig. 5. EDX spectrum (a) raw crab shell and (b) acidized crab shell.

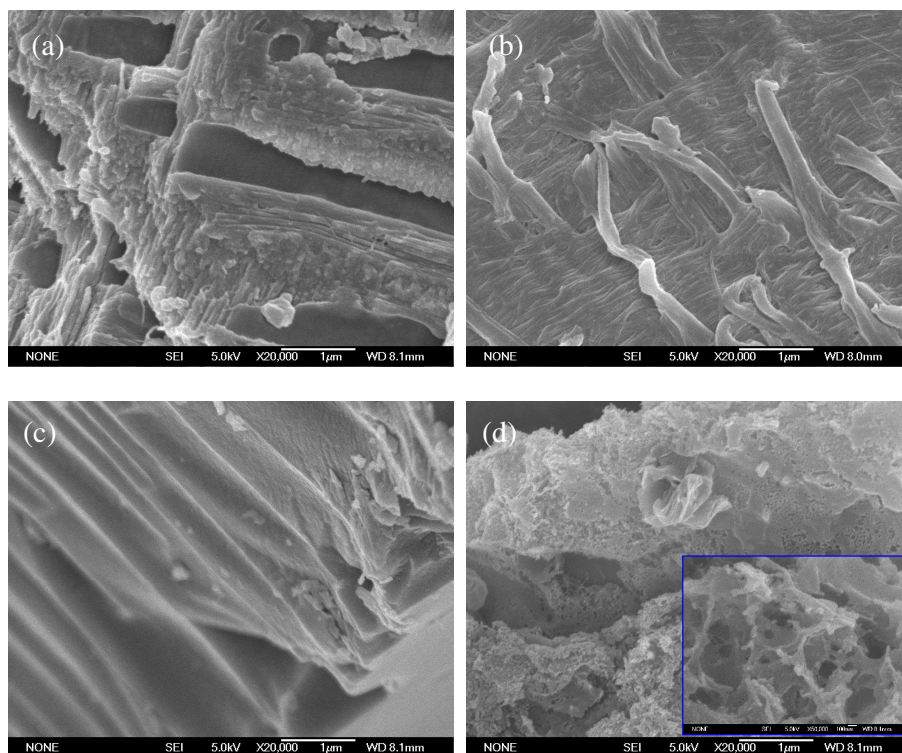


Fig. 6. Scanning electron microscopy image of (a) raw crab shell, (b) acidized crab shell, (c) carbonized crab shell and (d) crab shell activated carbon ($\times 20000$).

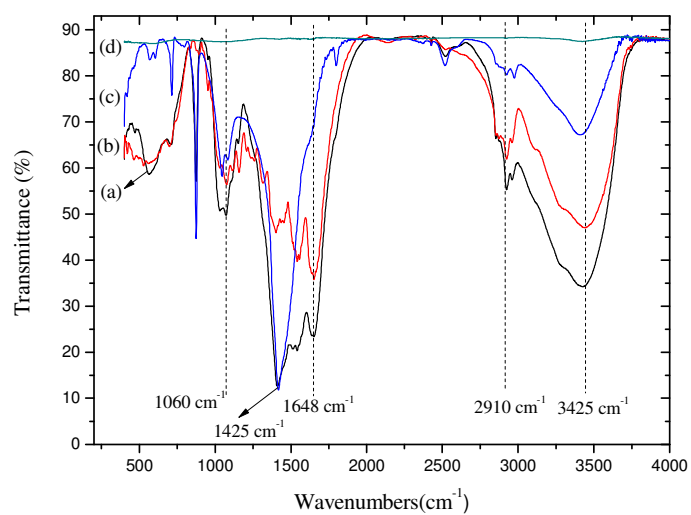


Fig. 7. FTIR spectra of (a) raw crab shell, (b) acidized crab shell, (c) carbonized crab shell and (d) crab shell activated carbon.

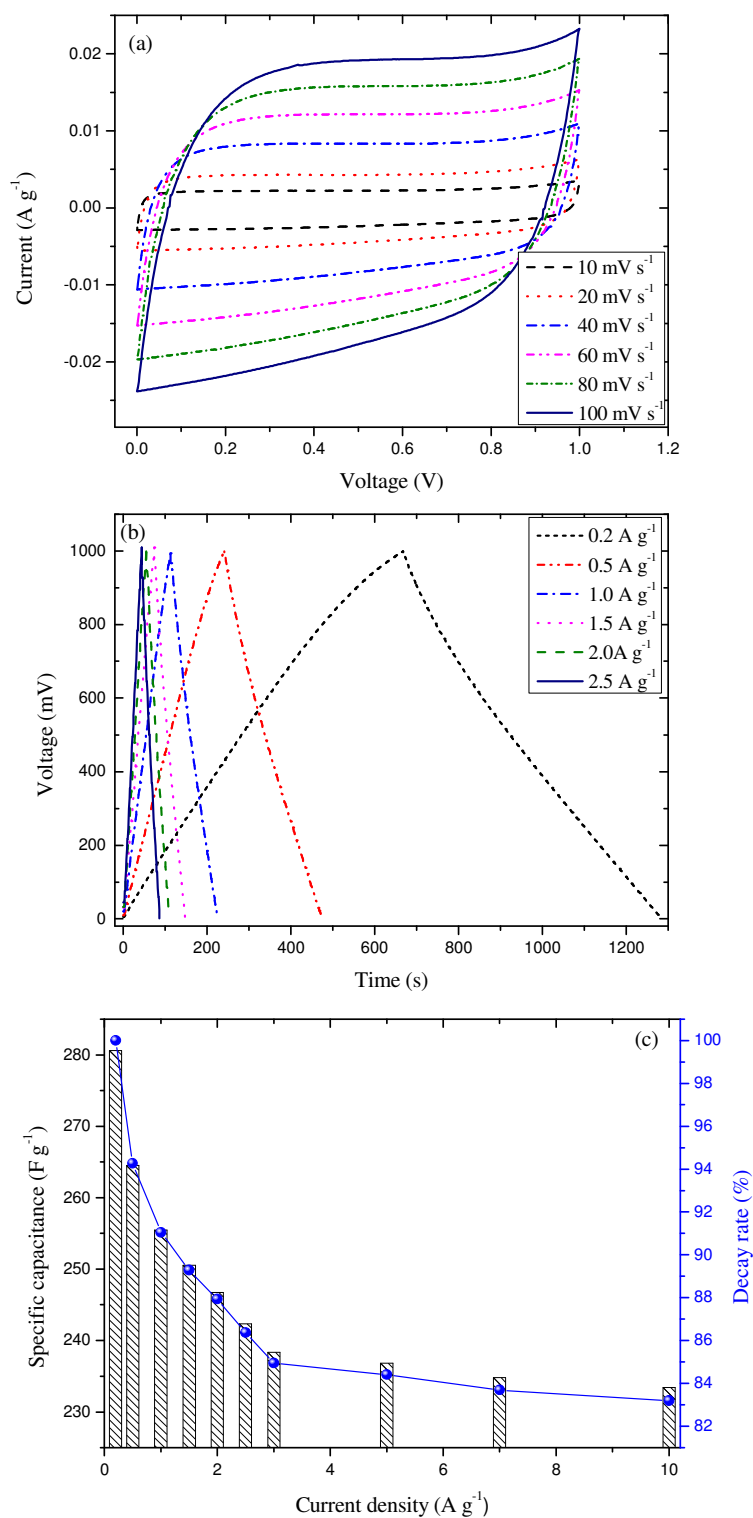


Fig. 8. (a) Cyclic voltammograms at different scan rates, (b) charge/discharge curves and (c) the specific capacitance at various current densities of CSAC-3 electrodes.

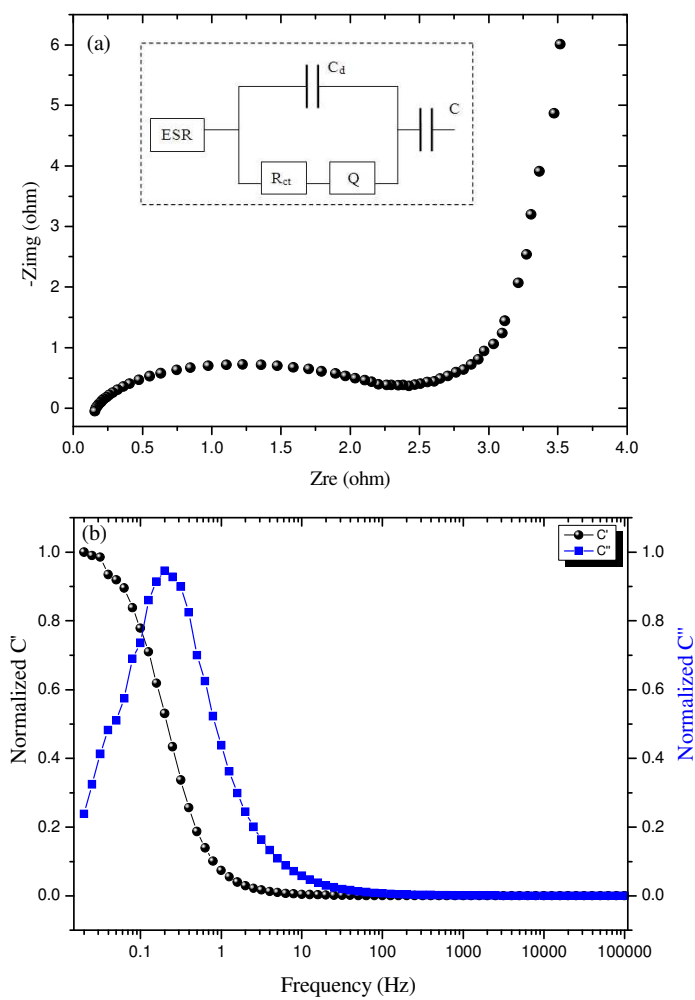


Fig. 9. (a) Nyquist impedance plots and normalized real and imaginary part capacitance of the CSAC-3 electrodes.